



Aalborg Universitet

AALBORG UNIVERSITY
DENMARK

Tvindkraft: Implementing a 500 kW 21-IGBT-Based Frequency Converter for a 1.7 MW Wind Power Conversion System

Gonzalez, Pablo Casado; Pang, Ying; Reigosa, Paula Diaz; Dimopoulos, Emmanouil; Barreras, Jorge Varela; Schaltz, Erik

Published in:

Proceedings of the 2013 IEEE International Conference on Renewable Energy Research and Applications

DOI (link to publication from Publisher):

[10.1109/ICRERA.2013.6749803](https://doi.org/10.1109/ICRERA.2013.6749803)

Publication date:

2013

Document Version

Accepted author manuscript, peer reviewed version

[Link to publication from Aalborg University](#)

Citation for published version (APA):

Gonzalez, P. C., Pang, Y., Reigosa, P. D., Dimopoulos, E., Barreras, J. V., & Schaltz, E. (2013). Tvindkraft: Implementing a 500 kW 21-IGBT-Based Frequency Converter for a 1.7 MW Wind Power Conversion System. In *Proceedings of the 2013 IEEE International Conference on Renewable Energy Research and Applications* (pp. 482-487). IEEE Press. <https://doi.org/10.1109/ICRERA.2013.6749803>

General rights

Copyright and moral rights for the publications made accessible in the public portal are retained by the authors and/or other copyright owners and it is a condition of accessing publications that users recognise and abide by the legal requirements associated with these rights.

- ? Users may download and print one copy of any publication from the public portal for the purpose of private study or research.
- ? You may not further distribute the material or use it for any profit-making activity or commercial gain
- ? You may freely distribute the URL identifying the publication in the public portal ?

Take down policy

If you believe that this document breaches copyright please contact us at vbn@aub.aau.dk providing details, and we will remove access to the work immediately and investigate your claim.

Tvindkraft: Implementing a 500 kW 21-IGBT-Based Frequency Converter for a 1.7 MW Wind Power Conversion System

Pablo Casado González, Ying Pang, Paula Díaz Reigosa,
Emmanouil Dimopoulos, Jorge Varela Barreras, Erik Schaltz

Department of Energy Technology, Aalborg University
Aalborg, Denmark

pgonza10@student.aau.dk, ypang12@student.aau.dk, pdiazr12@student.aau.dk

Abstract—The 54-meter-high Tvindkraft windmill was built by a group of volunteers during 1975-1978, as an argument for renewable energy sources as well as an argument against nuclear power. At that time it was the world's biggest windmill. So far, Tvindkraft has been running for 35 years, proving that a well-constructed wind turbine is a sustainable approach to renewable energy utilization. This paper deals with the analysis, simulation, implementation and experimental testing of a new 500 kW 21-IGBT-based frequency converter that will run in parallel with the former 12-Thyristor-based frequency converter to fully utilize the capacity of the windmill. Simulations and experimental results are presented side-by-side to verify the proper functionalities of the frequency converter described in this paper.

I. INTRODUCTION

In the past numerous energy harvesting systems, associated with variable-speed wind power systems, have been introduced [1-5] and while a fair amount of them had a great impact on the wind power industry applications, others were quickly rendered obsolete due to excessive economic cost, grid-codes requirements and other limitations. In this paper, a 500 kW frequency converter, designed based on a compromise between reduced economic cost and antagonistic operation, is thoroughly discussed.

The 21-IGBT-based frequency converter is employed to support the connection of a 1.7 MW Wound Rotor Synchronous Generator (WRSG), installed in the windmill's hub, to the grid, by operating in parallel with a 500 kW 12-Thyristor-based frequency converter. The remaining power is used for auxiliary systems, e.g. heating.

A simplified diagram of the frequency converter, consisting of a three-phase passive rectifier, a three-leg boost converter, a three-phase two-level Pulse-Width-Modulated Voltage Source Inverter (PWM-VSI) and an LCL-filter, is illustrated in Fig. 1.

The entire frequency converter has the following important advantages:

- The frequency converter accepts the output of the synchronous generator at various frequencies, which allows the wind turbine to operate in a variable-speed range and achieve maximum aerodynamic efficiency.
- The DC-link decouples the generator side from the grid side, rendering feasible the fixed-frequency feeding of the grid, even though the frequency and the magnitude of the generator voltage may vary significantly.
- Additionally, with fully controllable devices, the frequency converter is able to control both the active and reactive power fed to the grid and therefore reactive power compensation is also achievable.

A thorough description of the frequency converter is presented in Section II. A model of the frequency converter has been developed and simulated in MATLAB® block diagram environment (Simulink®) using PLECS® blockset as well. The performance of the model is verified in Section III. Furthermore, in Section IV, and in order to testify the proper behavior of the real system, field test experiments are presented and compared side-by-side with the respective simulation results of Section III.

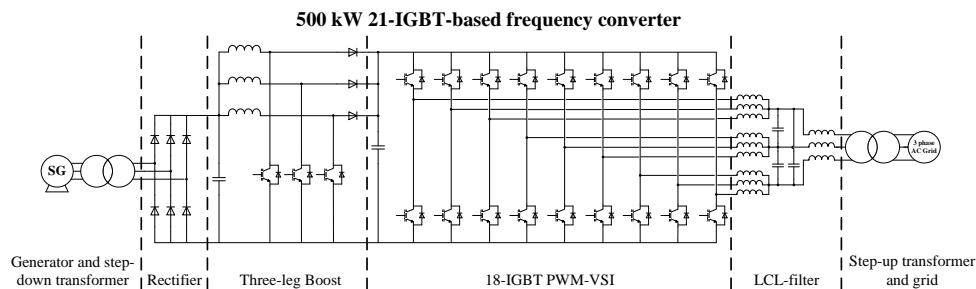


Figure 1. Simplified diagram of the 500 kW 21-IGBT-based frequency converter built in Tvindkraft.

II. DESCRIPTION OF THE 21-IGBT-BASED FREQUENCY CONVERTER

A. Three-phase Passive Rectifier

The AC power generated by the WRSF, the frequency and magnitude of which are varying along the wind speed variations, is rectified by a three-phase passive rectifier. An additional RC snubber branch has been installed in parallel with each diode to limit the latter's one maximum voltage stress, during the turn-off transient, under the presence of stray inductances [6].

B. Three-leg Boost Converter

The output DC voltage of the passive rectifier varies according to the wind speed and thereby the voltage of the DC-link which is the input voltage of the PWM-VSI will be unstable without dedicated control. Such instability may cause a fault operation of the VSI when the DC-link voltage is lower than a certain value. Therefore, in order to ensure that the input voltage of the VSI is high enough, a three-leg boost converter is employed. The installed topology lowers the current flowing through the IGBTs, and thereby mitigates the overheat problem of these devices.

The control strategy of the three-leg boost converter is based on the Current Programmed Control (CPC) mode with variable ramp compensation (Fig. 2), which is implemented to ensure the stability of the system whenever the duty cycle exceeds 0.5, by dynamically adjusting the slope magnitude, as discussed in [4, 7]. The boost converter regulates the inductor current i_L so the requested power P_{set} is delivered to the inverter. The processor calculates the requested power taking into account the current, the rotor speed and the wind speed. Furthermore, the reference current I_{ref} is calculated by subtracting the maximum current by the artificial ramp.

C. 18-IGBT-based PWM-VSI Inverter

1) Topology of the inverter

As shown in Fig. 1, the inverter consists of 18 IGBTs and essentially it operates as three three-leg inverters in parallel.

The purpose of this design is to reduce the current stress of each IGBT while keeping the DC-link voltage relatively low. On the other hand, the losses in the input inductors of the LCL-filter can also be reduced by 66.67 %.

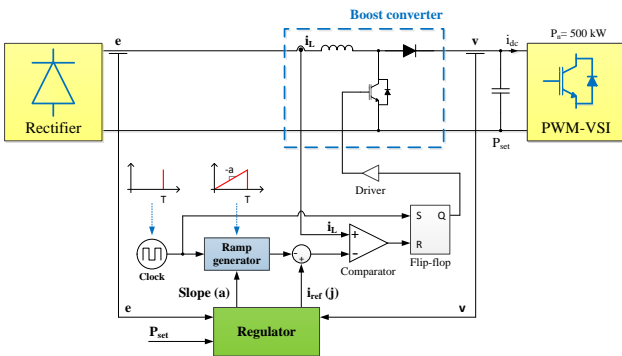


Figure 2. Single-leg equivalent diagram of the Current Programmed Control (CPC) strategy applied on the three-leg boost converter.

2) Control strategy of the inverter

Voltage Oriented Control (VOC) is applied on the inverter, which is based on the d-q frame [5], a phase-locked loop (PLL) [5] and PI regulation. The entire control is composed of two cascaded loops, i.e., current loop (inner loop) and voltage loop (outer loop).

a) d-q frame and PLL

In order to simplify the calculations for the control of the three-phase inverter, voltages and currents are transformed from a stationary abc reference frame into a synchronous rotating d-q reference frame. In this way the three-phase steady-state AC quantities are transformed into two DC quantities and PI controllers able to eliminate steady-state error can be implemented more straightforward. Furthermore, since there are coupling terms between the d and q axes, decoupling techniques are used to ensure an improved transient response. Similarly, the PLL is also based on the d-q frame [5].

The d-q frame voltage equations can be expressed as [8]

$$V_d = E_d + Ri_d + L \frac{di_d}{dt} - \omega Li_q, \quad (1)$$

$$V_q = E_q + Ri_q + L \frac{di_q}{dt} + \omega Li_d. \quad (2)$$

V_d and V_q are the d and q components of the output voltage of the inverter, E_d and E_q , are the d and q components of the grid voltage. Finally, R and L reflect the resistive and inductive components between the converter and the grid, taking into account the impedances of both the LCL-filter and the grid side transformer. The basic scheme of the cascaded controller is shown in Fig. 3. As it can be observed, the d-q frames of the current loops are coupled by the two terms $i_q\omega L$ and $i_d\omega L$, therefore two extra terms are added to decouple the frames ensuring the satisfactory performance of the PI regulator.

a) Current controller

After being decoupled, the d and q axis are independent and identical from the controller design point of view. Therefore only one axis will be discussed in the current controller.

A delay is introduced by the PWM sampling and computation time, which can affect the stability of the system by adding an extra pole to it [8]. Both the reference and feedback currents should be divided by 3 since there are three inverters in parallel and each one contributes to only 1/3 of the total current. This affects the gain of the control loops and it

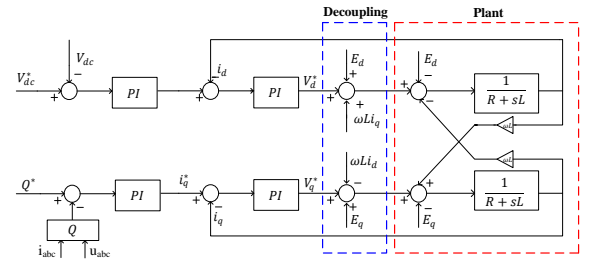


Figure 3. Scheme of the cascaded controller.

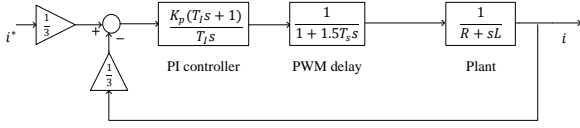


Figure 4. Block diagram of the current controller.

should be taken into consideration when tuning the parameters of the control to ensure the stability of the system. After all the factors are taken into account, the control block diagram of the current loop is shown in Fig. 4.

The technical optimum technique (i.e. 5 % overshoot) is used to properly tune the PI controller in the current loop [8]. Firstly, the integrator time constant is tuned to cancel the pole of lower frequency (in this case the pole introduced by the plant), since the current loop is designed to achieve fast response and high bandwidth. In this way, the integrator time constant T_i is calculated as

$$T_i = \frac{L}{R}. \quad (3)$$

After the integrator time constant is determined, only the proportional constant K_p needs to be tuned to achieve the indicated 5 % overshoot (i.e. the damping ratio = 0.707). As a result, it can be calculated as

$$K_p = \frac{L}{T_s}. \quad (4)$$

b) Voltage controller

The current loop is seen as a delay block from the voltage control loop. As the settling time of the current loop designed above is $9T_s$, it is viewed as a delay of $9T_s$, as shown in the control block diagram of the voltage control in Fig. 5.

According to [5], the plant transfer function of the voltage loop is

$$G_p(s) = \frac{\sqrt{3}R_i}{2(CR_i s - 1)}, \quad (5)$$

where R_i is the input equivalent resistance defined as $R_i = V_{dc}/i_{bst,0}$, and $i_{bst,0}$ is the current flow from the boost converter into the capacitor. Therefore the block diagram of the voltage loop can be developed as in Fig. 5.

The ‘‘optimum symmetrical’’ technique [9], is followed when tuning the PI in the voltage loop in order to ensure sufficient gain margin and phase margin at the same time.

The integrator time constant and the proportional constant were tuned as

$$K_p = 0.36 \cdot \frac{C}{T_s}, \quad (6)$$

$$T_i = 51 \cdot T_s. \quad (7)$$

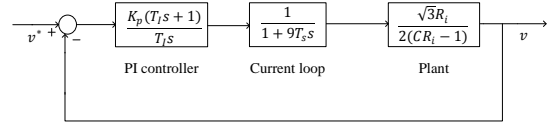


Figure 5. Block diagram of the voltage controller.

D. LCL-filter

Since the inverter operates as a voltage source, its interconnection to the grid is performed by means of an LCL-filter, which was designed based on [10]. The main aim of the filter is to mitigate the harmonic content [11], especially in the high frequency (HF) range of the spectrum, and also to provide a stable frequency response. Nonetheless, this type of topology introduces a resonance peak which should be damped to avoid instability [12]. The per-phase equivalent diagram of the filter is depicted in Fig. 6.

As shown in Fig. 6, the selected damping method is a resistor R_d in series with the capacitor C_f , and thus, a passive damping which introduces more losses to the system [13] but results in a more economical solution. The LCL-filter parameters are summarized in Table I (including the damping resistor). However, as the inverter per-phase current is divided by 3, the adopted topology differs from regular three-phase LCL filters and consists of nine converter-side inductors L_f (taking into account the calculated per-phase value).

In order to guarantee its stable response, it is crucial to analyze the LCL-filter in the frequency domain. Its transfer function, neglecting the internal resistance of the inductors, can be calculated from the circuit presented in Fig. 6

$$G_{LCL}(s) = \frac{i_g(s)}{v_{inv}(s)} = \frac{1}{L_f s} \cdot \frac{sR_d/L_g + 1/C_f L_g}{s^2 + C_f R_d \omega_{res}^2 s + \omega_{res}^2}, \quad (8)$$

where $\omega_{res}^2 = (L_g + L_f)/(L_g \cdot L_f \cdot C_f)$ [10]. The reader can observe in (8) that the damping resistor is adding a new zero to the transfer function of the system. Fig. 7 and Fig. 8 provide a clearer picture of the damping resistor influence.

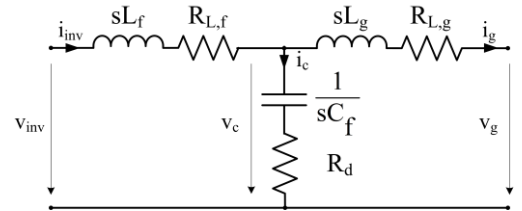


Figure 6. Block diagram of the voltage controller.

TABLE I. LCL-FILTER PARAMETERS

Parameter	Value
Converter side inductance L_f	25 [μ H]
Capacitor C_f	310 [μ F]
Damping resistor R_d	220 [m Ω]
Grid side inductance L_g	32 [μ H]

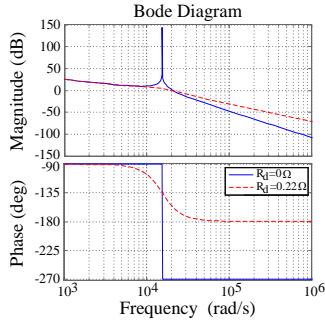


Figure 7. Bode plots of the LCL-filter transfer function with and without damping resistor (the applied value in the converter).

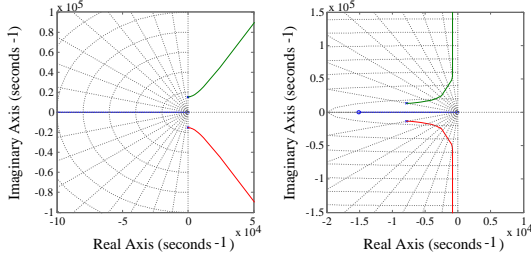


Figure 8. Root locus of the LCL-filter transfer function, without damping (left) and with series damping resistor (right).

The Bode diagram in Fig. 7 shows that the resonance peak is greatly damped and that the attenuation after the resonance is acceptable. On the other hand, the root locus in Fig. 8 demonstrates that the poles when the filter has no damping (left picture), which were located in the marginally stable region, are moved to the stable region (right picture).

III. SIMULATION RESULTS

A. Three-phase Passive Rectifier

Fig. 9 shows that for steady state operation the three-phase passive rectifier provides an output voltage, of which the frequency is six times as high as the frequency of the input voltage. Moreover the effect of the AC-side inductance is taken into account in the simulation and clearly seen in Fig. 9.

B. Three-leg Boost Converter

As stated before, the boost converter steps-up the input voltage up to 710 V to fulfill the input requirements of the PWM-VSI. The simulated waveforms presented in Fig. 10(a) verify that this objective is achieved. Furthermore, Fig. 10(b) proves that the CPC strategy of the boost converter ensures that the system is stable even when duty cycles are higher than 0.5 ($d > 0.5$). This simulation is performed during continuous mode operation and also shows that the currents are shifted 120°.

C. 18-IGBT Inverter

In order to examine the performance of the transient and steady state response of the VOC control, a step signal is set to be the active power reference stepping up by 250 kW at 0.12s and 0.275s, respectively. The reference value of the reactive

power is set to be 0. These reference signals and the output active and reactive power are plotted in Fig. 11(a), from which a tolerable overshoot of the output active and reactive power can be observed at the instant of the references step up.

The output DC-link voltage and its reference signal are plotted in Fig. 11(b). As it can be observed, the output follows the reference value at different power levels and even if deviates from the reference at the moment of the power step up, it soon decreases and follows the reference again.

The output i_d and i_q , together with their reference signals are plotted in Fig. 12(a), which demonstrates the fast response of the current controller as the output currents follow the reference instantaneously. In Fig. 12(b), phase A current and voltage are validated to be in phase, which satisfies the requirement of unity power factor.

D. LCL-filter

The inverter, capacitor branch and grid currents have been simulated at full-power (500 kW) in order to validate the correct performance of the filter. These quantities are presented in Fig. 13(a). In addition, the frequency spectrum (Fig. 13(b)) shows that the high frequency (HF) harmonics have been attenuated.

The LCL-filter simulation results agree with the concepts presented in Section II: HF harmonics around the switching frequency ($f_{sw} = 5$ kHz) have been dramatically reduced. Besides that, the total harmonic distortion (THD) obtained for the grid currents, 1.61%, is well below the grid codes (Table II) [11].

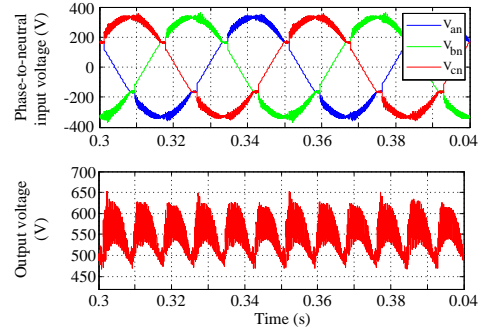


Figure 9. Simulated waveforms of the three-phase passive rectifier: phase-to-neutral input voltages (upper) and DC output voltage (lower).

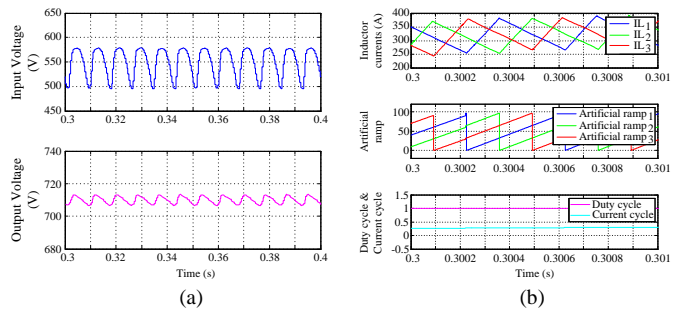


Figure 10. Simulated waveforms of the three-leg boost converter: (a) Input and output voltages, (b) Inductor currents and artificial ramps of the three legs, current and duty cycle.

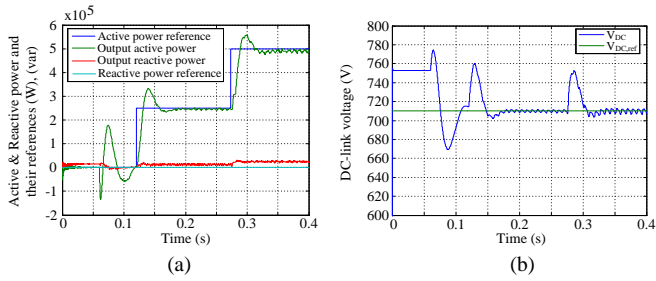


Figure 11. Simulated waveforms of the 18-IGBT inverter: (a) active and reactive power and their references, (b) DC-link voltage and its reference.

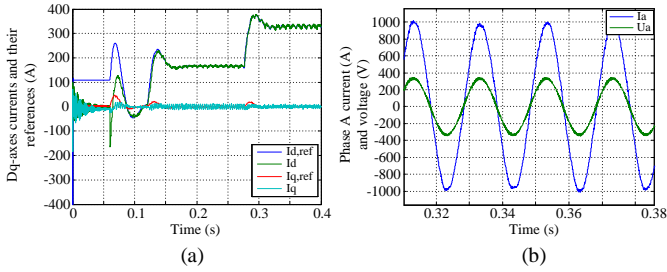


Figure 12. Simulated waveforms of the 18-IGBT inverter: (a) dq-axis currents and their references, (b) phase A voltage and current.

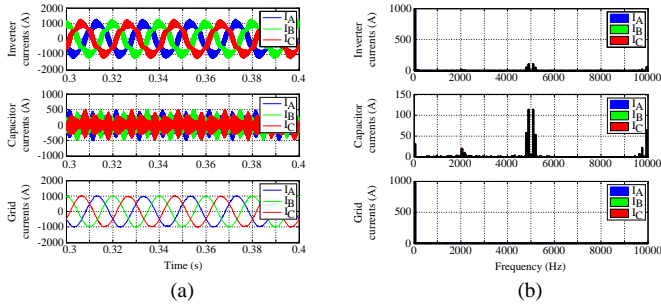


Figure 13. Simulated input, capacitor branch and grid currents of the LCL-filter: (a) Time-domain waveforms, (b) Frequency spectrum.

TABLE II. THD OF THE SIMULATED INPUT AND GRID CURRENTS

Input current, THD	Grid current, THD
20,61 %	1,62 %

IV. EXPERIMENTAL RESULTS

Finally, Section IV presents the validation of the proper operation of the frequency converter and the concepts previously introduced in Section II. The 500 kW frequency converter located in Tvindkraft is depicted in Fig. 14.

A. Three-phase Passive Rectifier

Fig. 15 illustrates the measured line-to-line input voltage and output voltage of the passive rectifier, which are in a good agreement with the waveforms obtained via simulations.

B. Three-leg Boost Converter

In order to prove that the control strategy of the boost converter (CPC) behaves correctly along different operating

points, the measurements are triggered for two modes of operation: continuous and discontinuous mode. Fig. 16 represents that for both modes of operation the system is stable. The continuous mode is reached when the power delivered to the grid is relatively high (100 kW). On the other hand the discontinuous mode is achieved when the power delivered to the grid is lower (30 kW).

C. 18-IGBT Inverter

In the field tests, the output active and reactive power, DC-link voltage, i_d and i_q , grid current and grid voltage have been measured. As it can be observed in Fig. 17 and Fig. 18, the implemented inverter is operating as expected, being in a good accordance with the simulations and the design of the controller.

D. LCL-filter

Similarly to Section III, the LCL-filter currents have been measured via field tests (Fig. 19(a) and Fig. 19(b)).

The results show that the switching frequency ripple has been reduced (Fig. 19(a)). Additionally, the frequency spectrum in Fig. 19(b) illustrates the mitigation of the HF harmonics, which is the main task of the LCL-filter. However, even though the measured THD of the grid current is 10.54%, exceeding the grid code requirements, further research on its frequency spectrum is considered crucial, as in this experiment the FFT analysis was made on a stepped-down signal supplied through LEM modules, in contrast with the input and capacitor branch filter currents which were measured with the use of typical Rogowski coils.

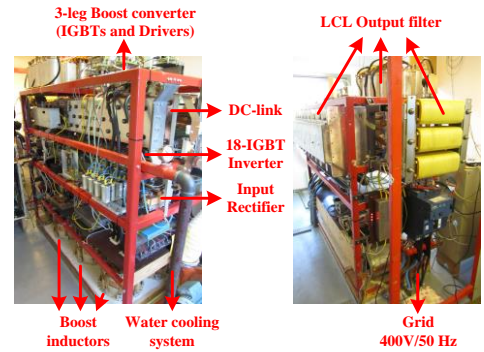


Figure 14. 500 kW 21-IGBT-based frequency converter built in Tvindkraft.

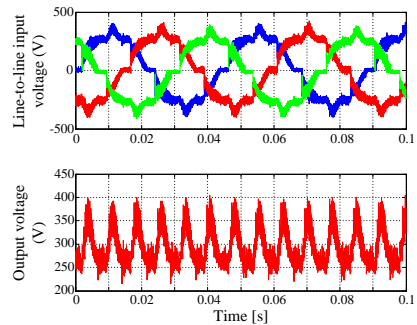


Figure 15. Passive rectifier measurements: line-to-line input voltage (upper plot) and rectified output voltage (lower plot).

ACKNOWLEDGMENT

The authors acknowledge Allan L. Jensen and Britta E. Jensen from Tvindkraft for selflessly granting us access to the Tvindkraft system and for all their help during the field tests.

V. CONCLUSIONS

This paper has provided a comprehensive description of the 500 kW 21-IGBT-based frequency converter installed in the 1.7 MW Tvindkraft windmill. The proper performance of the system has been verified by means of simulation and field test results. The obtained results confirm that the entire converter is working as described in Section II. Therefore, it is concluded that the topologies and control strategies presented through this paper are a feasible and reliable solution for a non-commercial MW-level wind power system such as Tvindkraft. As future work, an analysis of the system and its efficiency with the new step-up transformer installed in the generator side should be done to verify the expected improvements.

REFERENCES

- [1] H. Li, Z. Chen, "Overview of different wind generator systems and their comparisons," *IET Renewable Power Generation*, vol.2, no.2, pp.-123-138, Jun. 2008.
- [2] Z. Chen, J.M. Guerrero, F. Blaabjerg, "A Review of the State of the Art of Power Electronics for Wind Turbines," *IEEE Transactions on Power Electronics*, vol.24, no.8, pp.1859-1875, Aug. 2009.
- [3] M. Liserre, R. Cárdenas, M. Molinas, J. Rodríguez, "Overview of Multi-MW Wind Turbines and Wind Parks", *IEEE Transactions on Industrial Electronics*, vol. 58, no.4, Apr. 2011.
- [4] X. Xiong, H. Liang, "Research on multiple boost converter based on MW-level wind energy conversion system," *Proceedings of the Eighth International Conference on Electrical Machines and Systems*, 2005. ICEMS 2005. Vol.2, no., pp.1046-1049 Vol. 2, 29 Sep. 2005.
- [5] R. Teodorescu, M. Liserre, P. Rodríguez. *Grid Converters for Photovoltaic and Wind Power Systems*. John Wiley and Sons, Ltd., 1st edition, 2011.
- [6] N. Mohan, T. M. Undeland, and W. P. Robbins. *Power Electronics: Converters, Applications and Design*. John Wiley & Sons, Inc., 3rd edition, 2003.
- [7] R.W. Erickson, D. Maksimovic. *Fundamentals of power electronics*. Kluwer Academic Publishers, 2nd edition, 2001.
- [8] M. Liserre, A. Dell'Aquila, F. Blaabjerg, "Design and control of a three-phase active rectifier under non-ideal operating conditions," *Conf. Rec. IEEE-IAS Annual Meeting*, vol.2, pp.1181-1188, 2002.
- [9] W. Leonhard. *Control of electrical drives*. Springer, 1997. ISBN 3540593802.
- [10] M. Liserre, F. Blaabjerg, S. Hansen, "Design and control of an LCL-filter based three-phase active rectifier," *Proc. of Industry Applications Conference*, 2001. Thirty-Sixth IAS Annual Meeting.vol.1, no. 1, pp.299-307, Sep. 30 2001-Oct. 4 2001.
- [11] IEEE Std. 519-1992. *IEEE Recommended Practices and Requirement for Harmonic Control in Electrical Power Systems*, IEEE Industry Applications Society / Power Engineering Society, 1992.
- [12] M. Liserre, A. Dell'Aquila, F. Blaabjerg, "Stability improvements of an LCL-filter-based three-phase active rectifier," *Proceedings of PESC 2002*, pp.1195-1201, Jun. 2002.
- [13] R. Peña-Alzola, M. Liserre, F. Blaabjerg, R. Sebastián, J. Dannehl, F.W. Fuchs, "Analysis of the Passive Damping Losses in LCL-Filter-Based Grid Converters," *IEEE Transactions on Power Electronics*, vol.28, no.6, pp.2642-2646, Jun. 2013.

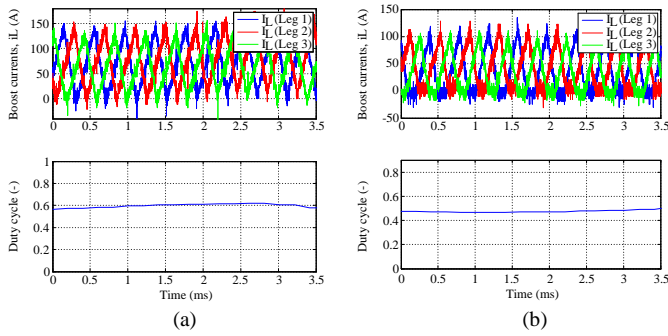


Figure 16. Measured waveforms in the three-leg boost converter:
 (a) Inductor currents (upper) and duty cycle (lower) for continuous mode,
 (b) Inductor currents (upper) and duty cycle (lower) for discontinuous mode.

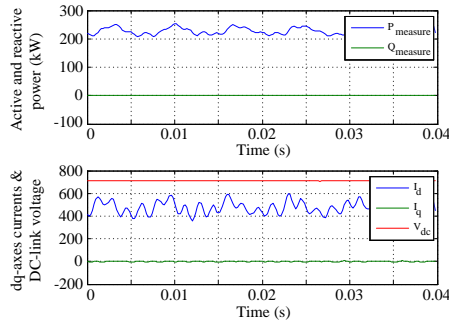


Figure 17. Measured waveforms of the 18-IGBT inverter: active and reactive power (upper), i_d , i_q and DC-link voltage (lower).

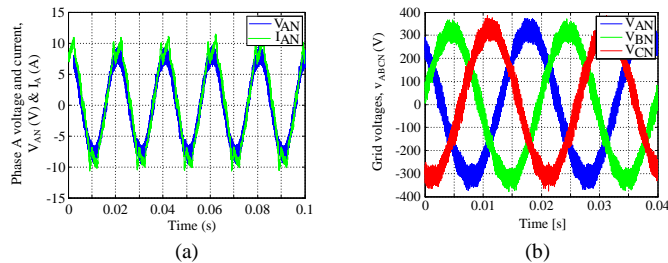


Figure 18. (a) Measured current and voltage of phase A of the 18-IGBT inverter, (b) Measured three-phase grid voltages.

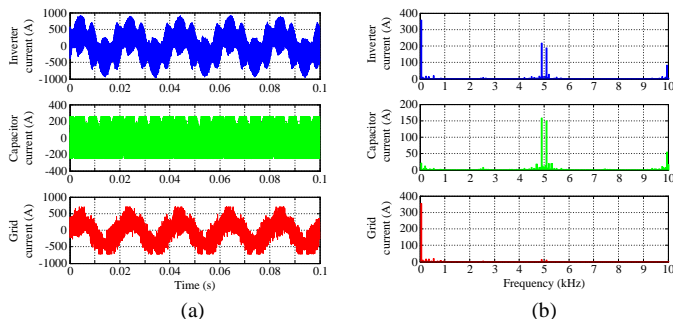


Figure 19. Measured input, capacitor branch and grid currents of phase C of the LCL-filter: (a) Time-domain waveforms, (b) Frequency spectrum.